# Path Instabilities of Rising Air Bubbles in a Hele-Shaw Cell

Erin Kelley and Mingming Wu*
*Department of Physics, Occidental College, Los Angeles, California 90041*
(Received 22 April 1997)

The path of a circular air bubble rising in a viscous fluid of a Hele-Shaw cell is found to change from a straight path to a zigzag path when the Reynolds number of the bubble (proportional to the bubble terminal velocity) exceeds a threshold. By visualizing the wake structures of the rising bubbles, and measuring the actual paths of the bubbles, we demonstrate that the path instability is a consequence of the vortex shedding behind the bubble. [S0031-9007(97)03801-5]

PACS numbers: 47.55.Dz, 47.20.Ft, 47.27.Vf

Much of the work on the motion of the air bubbles rising in a fluid medium has focused on the study of the terminal velocity and the drag force [1–4]. Very little attention has been paid to the path instabilities of the rising air bubbles [5–8]. It is known that the path of a rising bubble in a bulk fluid changes from a straight path to a spiral or zigzag path when the size of the bubble exceeds a critical value. The first such observation was reported nearly four decades ago by Haberman and Morton [2]. They conjectured that "the oscillatory motion of the bubbles is probably caused by the periodic shedding of vortices behind the bubble." Subsequently, several extensive analytical and experimental studies [5–7] were done on the path instabilities of the rising air bubbles. Reynolds number and Weber number (related to the deformation of the bubble) were found to be the controlling parameters of the path instabilities. However, no consistent stability criteria can be found in the current literature. To the authors' knowledge, the exact nature of the zigzag instability is yet unknown.

Recently, Maxworthy *et al.* [9] did beautiful work on the motion of air bubbles rising in a Hele-Shaw cell filled with silicone oil. In their study, the air bubbles were flattened on both sides by glass plates; consequently, the motion of the bubbles was two dimensional. Their work focused on the shape and the terminal velocity of the rising bubbles. Considering the simplicity introduced by the 2D motion of the bubbles, we adopted Maxworthy *et al.*'s experimental setting to study the path instabilities of the rising bubbles. Similar to the case of air bubbles rising in a bulk fluid, the paths of the bubbles rising in a Hele-Shaw cell are controlled by both Reynolds number and Weber number. For the experimental studies shown below, we focused on the study of path instabilities as a function of Reynolds number, while keeping the Weber number at a small value. The small Weber number was easily achieved using small air bubbles together with water as the fluid medium. As a result, the deformations of the bubble surfaces were negligible.

In this Letter, we report experimental studies of the path instabilities of the flattened air bubbles rising in a Hele-Shaw cell. Our experimental results demonstrate that the path of a circular bubble changed from a straight path to a zigzag path when the Reynolds number $R$ of the bubble exceeded a threshold $R_c$. The Reynolds number is defined as $R = Ud/\nu$, where $U$ is the terminal velocity of the bubble along the center line of the path, $d$ is the bubble diameter, and $\nu$ is the kinetic viscosity of the ambient fluid. The zigzag motion of the bubble was found to be a consequence of the *vortex shedding* behind the air bubble. Consistent results were obtained using two different experimental methods. In the first method, we obtained the curve of Strouhal versus Reynolds number (Strouhal curve) of the path of the rising bubble. The Strouhal number St is defined as $fd/U$, where $f$ is the zigzag frequency of the path. The resulting curve was found to be similar to the Strouhal curve obtained in the wake of a solid cylinder [10,11]. We also measured the amplitude of the zigzag path as a function of Reynolds number. The amplitude squared was found to be proportional to $R$ near the onset of the path instability, a good indication of a supercritical bifurcation [12,13]. In the second method, wake structures behind the air bubble were visualized using a dye visualization technique. For a bubble that followed a straight path, two symmetric vortices were observed attached to the rear of the bubble. For a bubble that followed a zigzag path, the vortices were detached from the rear of the bubble and shed into the ambient fluid periodically. The latter is reminiscent of a well known phenomenon, the Kármán vortex street in the wake of a solid cylinder [14,15].

The main part of the experimental apparatus was the Hele-Shaw cell. It consisted of two parallel rectangular glass plates (15 in. $\times$ 38.5 in. $\times$ 1/4 in.), separated by a $\frac{1}{16}$ in. thick Teflon spacer. Viscous fluid (doubly deionized and distilled water) filled between the two glass plates. Extreme cautions were taken to keep the cell as clean as possible. Large bubbles were driven through the cell for removing the surface-active contaminants prior to each experimental run. A piece of O-ring stock (Buna-N) was aligned along the Teflon spacer to provide a seal. The two glass plates were than placed on a rigid aluminum frame and were pressed together by clamps at the edges. The gap between the two glass plates was $h = 0.162 \pm 0.003$ cm. The frame was supported by a stand, where it could be tilted at different angles $\alpha$. Air bubbles were injected through a Teflon tube that was placed along the

 © 1997 The American Physical Society 

center line at the lower end of the cell. The velocity of the rising bubble was controlled by the tilt angle of the cell and the bubble size. A Hamilton syringe dispenser (PB-600) and a Hamilton syringe (total volume 500 $\mu$l) were used to generate bubbles of chosen sizes. For three experimental runs described below, the diameters of the bubbles were $d = 0.261 \pm 0.013$, $0.362 \pm 0.017$, and $0.448 \pm 0.004$ cm. Their corresponding aspect ratios $\Gamma$ ($= h/d$) were 0.621, 0.448, and 0.362. The temperature of the Hele-Shaw cell was $20.3 \pm 0.3°$ during the experimental runs. The kinetic viscosity $\nu = 0.009\,945$ cm$^2$/s and surface tension $\sigma = 72.70$ dyn/cm were given by Ref. [16].

The shapes and the paths of the bubbles were recorded separately by two CCD cameras. The Hele-Shaw cell was lit up by a diffused light from below, and the cameras were mounted above the center line of the cell. The first camera was attached to the frame, and was placed close to the bubble injection point to take a close-up image of the bubble. The image contained $640 \times 480$ pixels and covered an area of $2.36 \times 1.77$ cm. The second camera was mounted farther away for recording the path of the air bubble. The image contained $640 \times 200$ pixels and typically covered an area of 20.5 cm $\times$ 6.40 cm. This area varied slightly among the runs for different tilt angles, since the camera was not attached to the frame. For a typical experimental run, an air bubble of chosen size was released at the bottom of the Hele-Shaw cell, and the bubble rose along the center line of the cell. A close-up image of the bubble was first recorded by a S-VHS VCR via the first camera at a location ~5 cm away from the bubble injection point. The image was used to determine the diameter and the shape of the bubble at a later time. The bubble then traveled about 20 cm before it entered the viewing field of the second camera. A series of 50 images was taken by the second camera together with an image grabbing board. The time between two consecutive images was $\frac{1}{15}$ s (each image contained two fields, the even field and odd field, and the two fields were $\frac{1}{60}$ s apart). The outline of the bubble in each image was extracted by finding the $x$-$y$ coordinates of those pixels with gray scales lower than a threshold value. The center of the bubble outline was used as the position of the bubble. We obtained the path of the bubble by plotting the positions of all the bubbles in an image series on one plot. The dotted lines in Fig. 1 were the paths of the bubbles at several different Reynolds numbers. For Reynolds number below the onset [see Fig. 1(a)], the bubble rose along the $y$ axis via a nearly straight path. The scatters along the horizontal direction ($x$ axis) were less than one pixel. For Reynolds number above onset [see Figs. 1(b) and 1(c)], the paths of the bubbles became zigzag. The experimental data fitted surprisingly well to zigzag functions as shown by the solid lines. Comparing Fig. 1(b) with Fig. 1(c), one finds that the amplitudes of the zigzag path increased with the Reynolds number. At the top of Fig. 1, there are three actual close-up images of the bubbles corresponding to each path shown below. They demonstrate that the bubbles at these three Reynolds numbers were nearly circular.

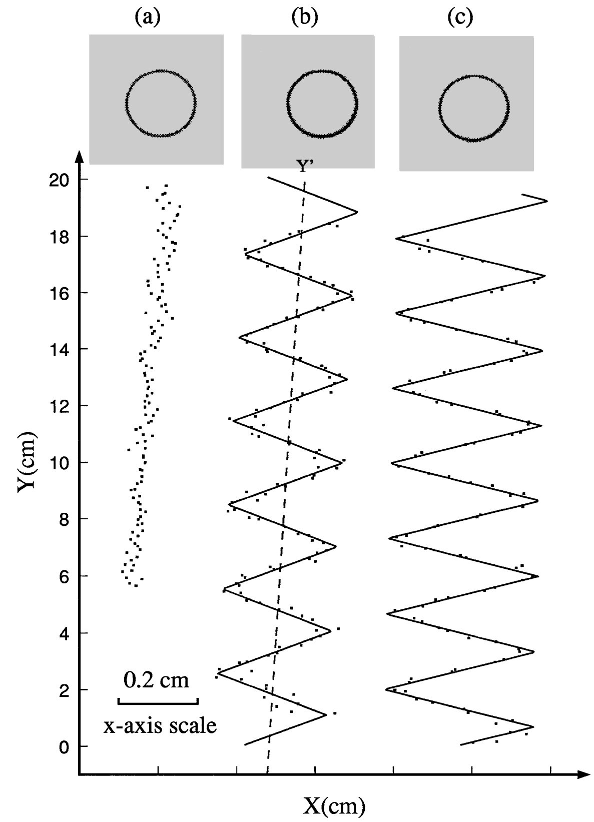


FIG. 1. Paths of bubbles with diameter $d = 0.362 \pm 0.017$ cm rising along the $y$ axis at each of the three Reynolds numbers. (a) $R = 137$, (b) $R = 171$, (c) $R = 205$. $x$ axis represents the horizontal position of the bubble. Dots are the positions of the bubbles extracted from the image series; solid lines are fits to zigzag functions. The dashed line indicates the center line of the bubble path. The top images are the three close-up images of the bubbles with arbitrary units.

The zigzag function that we used to fit the data in Figs. 1(b) and 1(c) contained five adjustable parameters. The two most important parameters are $\tilde{A}_0$, the amplitude of the zigzag path, which describes the maximum displacement of the bubble along the horizontal direction (the $x$ axis) and $T$, the period of the zigzag path, which describes the distance from peak to peak along the center line of the path [see Figs. 1(b) or 1(c)]. The other three parameters were of minor interest to us; they were introduced to account for the initial position of the bubble $(x_0, y_0)$ when it enters the viewing field of the camera, and also the slope $k$ which describes the deviation of the path center line $y'$ axis from the $y$ axis.

In Fig. 2, we plotted the distances that the bubbles traveled along the center line of the path as a function of time at several tilt angles. Data points were from experiments. Solid lines were fits to straight lines. Bubble velocities were given by the slopes of the fitted lines. As seen, the velocities were very constant in the range where the image series was taken. Here we made an attempt to compare our experimentally measured velocities to those calculated

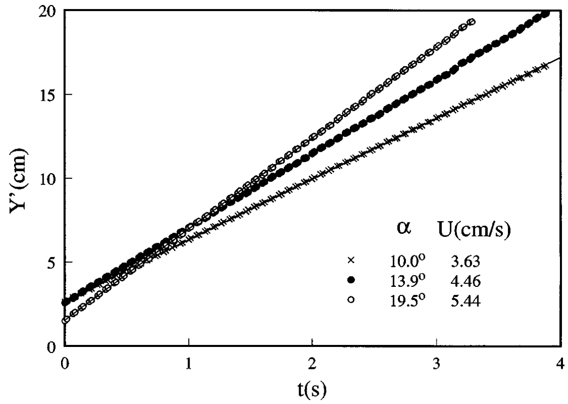


FIG. 2. Distance that the bubbles ($d = 0.362 \pm 0.017$ cm) travel along the center line of the cell as a function of time at several tilt angles $\alpha$. Data points are experimental data; solid lines are fits to straight lines. The slope of the line gives the velocity $U$ of the bubble.

from the theory. For the bubble that follows a straight path in Fig. 1(a), we obtained a rising velocity of 3.63 cm/s. The bubble has a diameter of 0.362 cm and rises at a tilt angle of 10.0°. Maruvada *et al.* [17] derived a formula for velocities of bubbles rising in a Hele-Shaw cell using a nonslip boundary condition. Using Eq. (15) of Ref. [17], we obtained a velocity of 0.168 cm/s at a tilt angle of 10.0°, an order of magnitude smaller than the experimental value of 3.63 cm/s. We also used the formula derived by Tanveer [18] for the velocities of bubbles rising under the pressure gradient in a viscous fluid of a Hele-Shaw cell. We obtained a theoretical value of 37.4 cm/s, a magnitude larger than the experimental value. The theoretical formulas in Refs. [17,18] suggest that the velocity of a circular rising bubble does not depend on the bubble size, while experimentally, we observed a strong dependency.

By fitting the path of the bubble to a zigzag function as shown by the solid line in Figs. 1(b) or 1(c), we obtained the period $T$ of the zigzag path, thus the Strouhal number, $\mathrm{St} = fd/U = d/T$. The Strouhal curves for bubbles of several sizes are shown by the scattered lines in Fig. 3(a). The solid lines in Fig. 3(a) are fits to $A/R + B + CR$. The purpose of the fitting is to compare our experimental results to the Strouhal curves obtained in the wake of a solid cylinder [10,11]. Table I summarizes the fitted parameters $A$, $B$, and $C$ from the paths of the bubbles at three different sizes and the parameters obtained in the wake of a long solid cylinder. It needs to be noted that the comparison here is rather relative, since the flow fields around the air bubbles are more complicated than those of the solid cylinders due to the poiseuille flow introduced by the two glass plates. The aspect ratios of the air bubbles are much smaller than those of the solid cylinders. Table I shows that the fitted parameters $A$, $B$, and $C$ from the bubble paths are in the same order of magnitude as those from the wakes of the solid cylinders.

By fitting the path of a bubble to the zigzag function as shown by the solid line in Figs. 1(b) or 1(c), we obtained the amplitude $\tilde{A}_0$ of the zigzag path. For the

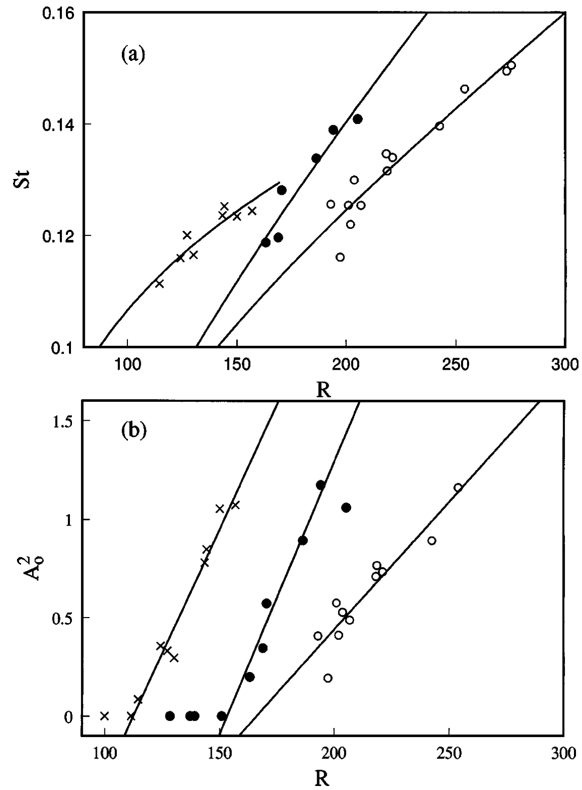


FIG. 3. (a) Curves of Strouhal vs Reynolds number. Solid lines are fits to $A/R + B + CR$. (b) Curves of dimensionless amplitude squared versus Reynolds number. Solid lines are fits to straight lines. Data points are from experiments for bubbles of three different sizes; $\times$, $d = 0.261$ cm; $\bullet$, $d = 0.362$ cm; $\circ$, $d = 0.448$ cm.

data shown below, we used a dimensionless amplitude $A_0$ which is scaled by the bubble diameter, $A_0 = \tilde{A}_0/d$. The dimensionless amplitude squared $A_0^2$ versus Reynolds number for bubbles of three different sizes is shown in Fig. 3(b). The data points are from the experiments, and the solid lines are fits to straight lines. As seen, $A_0^2$ is proportional to $R$, a good indication that the zigzag instability is a supercritical bifurcation. A similar linear relationship was found near the onset of vortex shedding in the wake of a solid cylinder [12,13]. The critical Reynolds number for the onset of the path instabilities was obtained by extrapolating the solid line in Fig. 3(b) to $A_0^2 = 0$. The values of $R_c$ for bubbles of three different aspect ratios are summarized in Table I. As seen, in the case of air bubbles, $R_c$ decreases when the aspect ratio $\Gamma$ increases, and all three values of $R_c$ for air bubbles are larger than 47.0, which is the $R_c$ for a long solid cylinder. In the case of a solid cylinder, it is known that $R_c$ decreases as the aspect ratio increases, and it approaches a value of 47.0 when $\Gamma$ is sufficiently large ($\Gamma \gtrsim 50$) [12].

We also studied the wake structures behind the bubble using a dye visualization technique. Colored food dye was used in our experiment and results at two different Reynolds numbers are shown in Fig. 4. For $R$ below

TABLE I. Comparison of our experimental results with those obtained in the wake of solid cylinders.

| $\Gamma$ | $R_c$ | $A$ | $B$ | $C$ |
|---|---|---|---|---|
| 0.362 (air bubble) | 166 | $-3.30$ | 0.0811 | $3.00 \times 10^{-4}$ |
| 0.448 (air bubble) | 153 | $-3.30$ | 0.0643 | $4.63 \times 10^{-4}$ |
| 0.621 (air bubble) | 113 | $-3.30$ | 0.126 | $1.36 \times 10^{-4}$ |
| $\geq$72 (solid cylinder) [10,12] | 47.0 | $-3.3265$ | 0.1816 | $1.600 \times 10^{-4}$ |

the onset [see Fig. 4(a)], the bubble follows essentially a straight path. The close-up image [see Fig. 4(c)] of the bubble shows that there are two symmetric (with respect to the center line of the bubble path) vortices attached to the rear of the bubble. For $R$ above the onset [see Fig. 4(b)], the bubble starts to zigzag, and the vortices formed behind the bubble are no longer symmetric, and they detach from the rear of the bubble one by one and shed into the ambient fluid periodically. The picture here is very similar to the one observed in the wake of a solid cylinder, known as Kármán vortex street [14,15].

The above experimental results show that the vortices were detached from the rear of the air bubble in a similar way that they were detached from the rear of a solid cylinder. A question to be addressed is whether the air bubble has a nonslip boundary as the solid cylinder at its surface. From the experimental evidences that we gathered, we conjecture that the small air bubbles described above may have nonslip boundary conditions. The rigid nature of the small air bubble was also observed among bubbles rising in a bulk fluid (water based) [2,4]. It was found that the curve of the drag force versus Reynolds number $R$ of the air bubble approached the drag curve of a rigid sphere at low Reynolds number. In order to examine the cause for the solidlike nature of our air bubbles, we repeated our experiments using tap water. No significant changes were observed within experimental errors for the terminal velocity of the air bubble or the critical Reynolds number for the onset of path instability. This indicates that the solidlike nature of the bubbles in distilled water may came directly from the large surface tension of the small bubble in water, not from the surface-active contaminants. Further experiments are in progress to determine the exact nature of the boundary condition at the bubble surface.

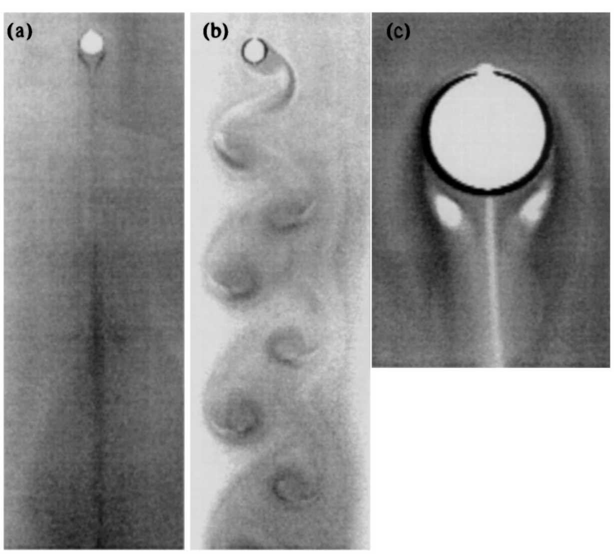


FIG. 4. Wake structures behind rising bubbles at two Reynolds numbers. (a),(c) $R = 102$, (b) $R = 222$.

In summary, we found that the straight path of a flattened circular bubble rising in a Hele-Shaw cell changed to a zigzag path when the Reynolds number exceeded a critical value. Our experimental results show that this path instability was caused by the vortex shedding in the wake of the bubble.

We thank Eric Moskun for assisting in data taking at a later stage of the experiment. Wu thanks M. Gharib and R. Henderson for very helpful discussions.

*Corresponding author.
Electronic address: mingming@oxy.edu

[1] R. Clift, J. R. Grace, and M. E. Weber, *Bubbles, Drops and Particles* (Academic, New York, 1978).
[2] W. L. Haberman and R. K. Morton, David Taylor Model Basin Report No. 802, 1953.
[3] D. W. Moore, J. Fluid Mech. **23**, 749 (1965).
[4] T. Maxworthy, C. Gnann, M. Kürten, and F. Durst, J. Fluid Mech. **321**, 421 (1996).
[5] P. G. Saffman, J. Fluid Mech. **1**, 249 (1956).
[6] R. A. Hartunian and W. R. Sears, J. Fluid Mech. **3**, 27 (1957).
[7] H. Tsuge and S. Hibino, J. Chem. Eng. Jpn. **10**, 66 (1977).
[8] G. Ryskin and L. G. Leal, J. Fluid Mech. **148**, 19 (1984).
[9] T. Maxworthy, J. Fluid Mech. **173**, 95 (1986).
[10] C. H. K. Williamson, Phys. Fluids **31**, 2742 (1988).
[11] M. Hammache and M. Gharib, J. Fluid Mech. **232**, 567 (1991).
[12] C. Mathis, M. Provansal, and L. Boyer, J. Phys. Lett. **45**, 483 (1984).
[13] M. Provansal, in *Propagation in Systems far from Equilibrium,* edited by J. E. Wesfreid, H. R. Brand, P. Manneville, G. Albinet, and N. Boccara (Springer-Verlag, Berlin, 1987), p. 354.
[14] D. J. Tritton, *Physical Fluid Dynamics* (Oxford Univ. Press, New York, 1988).
[15] Sadatoshi Taneda, J. Phys. Soc. Jpn. **11**, 302 (1956).
[16] R. C. Weast, *CRC Handbook of Chemistry and Physics* (CRC Press, West Palm Beach, FL, 1985), 64th ed.
[17] S. R. K. Maruvada and C.-W. Park, Phys. Fluids **8**, 3229 (1996).
[18] Saleh Tanveer, Phys. Fluids **29**, 3537 (1986).